



Delicate topotactic conversion of coordination polymers to Pd porous nanosheets for high-efficiency electrocatalysis

Zhenyuan Liu^a, Xiaoyu Yang^a, Bingqing Lu^a, Zhaoping Shi^a, Dongmei Sun^a, Lin Xu^{a,*},
Yawen Tang^a, Shuhui Sun^{b,*}

^a Jiangsu Key Laboratory of New Power Batteries, Jiangsu Collaborative Innovation Centre of Biomedical Functional Materials, School of Chemistry and Materials Science, Nanjing Normal University, Nanjing, 210023, PR China

^b Institut National de la Recherche Scientifique, Énergie Matériaux et Télécommunications, Varennes, QC, J3X 1S2, Canada



ARTICLE INFO

Keywords:

Coordination polymer
Topochemical reaction
Palladium
Porous nanosheet
Electrocatalyst

ABSTRACT

Two-dimensional noble metal-based nanosheets with high porosity represent a class of promising electrocatalysts due to their highly open structure feature, increased atomic utilization efficiency and thus boosted electrocatalytic performances. Nevertheless, it still remains greatly challenging to fabricate highly porous metal nanosheets through a feasible and general approach to date. Herein we present a novel coordination polymer (CP)-engaged approach to create a class of porous 2D Pd nanosheets for enhancing the electrocatalysis of small molecules through a two-step topotactic conversion reaction. The pre-synthesized Hofmann-type CP square nanoplates are firstly converted into Pd–Ni oxide through a mild calcination and eventually transformed into Pd porous nanosheets after repetitive cyclic voltammetry (CV) treatments in H_2SO_4 solution. Benefiting from intriguing structural advantages, the formed porous Pd nanosheets exhibit greatly improved catalytic performance toward the electrooxidation of liquid fuels (e.g., CH_3OH and $HCOOH$) and oxygen reduction reaction (ORR) as compared with commercial Pd black catalyst. The present synthetic strategy would provide a new perspective for the rational fabrication of noble metal-based porous nanosheets with extraordinary functionalities.

1. Introduction

As an important member of two-dimensional (2D) nanomaterial family, noble metal-based nanosheets have recently aroused tremendous research interests due to their unusual electronic structures and physiochemical properties [1–5]. As a consequence of 2D confinement and surface effect, noble metal-based nanosheets show great promising applications in various fields, including electrocatalysis [6–8], photothermal therapy [9,10], heterocatalysis [11,12], gas sensor [13,14], and memory devices [15], etc. Stimulated by these extraordinary properties, tremendous efforts have been devoted to preparing 2D noble metal-based nanosheets by different synthetic approaches, including self-assembly process [15–17], hard template-engaged method [18,19], capping agent-confined synthesis [7,20,21], photochemical synthesis [22,23], 2D oriented attachment [24,25], and so forth. However, the majority of the as-fabricated noble metal nanosheets appear as rigid nanostructure with smooth and intact surface, which tend to irreversibly restack during device fabrication and materials processing, resulting in a great loss of accessible surface atoms (Fig. 1a). [13,26] Such phenomenon would inevitably lead to a

detrimental impact on the utilization efficiency of noble metal atoms, especially in catalysis applications. In this regard, the porous nanosheets with rough surface and rich corner/edge atoms offer a very promising strategy for achieving outstanding catalytic performance in view of their remarkable features related to the high-efficiency utilization of both interior and exterior surface atoms as well as permeable channels for mass transport (Fig. 1b). To this end, rational synthesis of porous noble metal-based nanosheets is therefore highly demanded, yet still remains challenging.

Nanostructured coordination polymers (CPs) have been extensively served as versatile precursors to achieve various porous inorganic functional nanomaterials with controllable morphologies and tunable compositions which exhibit promising potentials in energy conversion and storage devices. [27–31] Nevertheless, the previously reported CP-derived nanomaterials mainly comprise porous carbon, transition metal oxides [29,32], chalcogenides [33] and phosphides [34], etc, rarely involving noble metal-based nanosheets. For the CP-derived fabrication of noble metal-based nanosheets, the synthetic challenges essentially lie in the following two aspects: (1) Due to the complicated coordination manners between different metal ions and organic bridged ligands, it is

* Corresponding authors.

E-mail addresses: xulin001@njnu.edu.cn (L. Xu), shuhui@emt.inrs.ca (S. Sun).

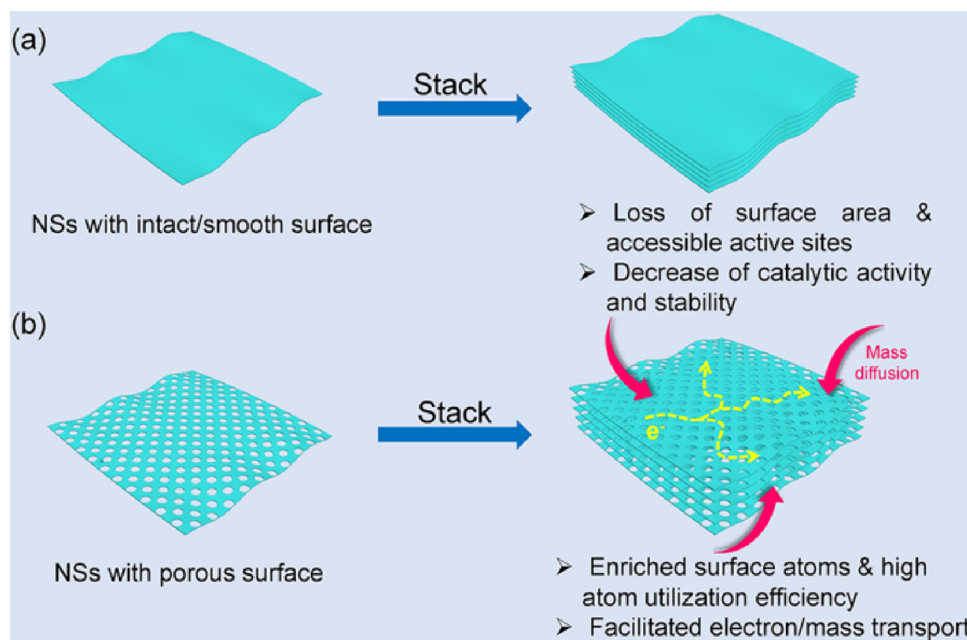


Fig. 1. Schematic illustration on demonstrating the stacking effect on electrocatalysis performance for noble metal nanosheets with different surface porosity.

still difficult to precisely synthesize noble metal-based CP nanosheets through a universal approach. (2) It is also difficult to perfectly maintain the 2D sheet-like nanostructure during the topotactic conversion from CP precursor to target noble metal because of the thin thickness of the CP precursor. Among various CPs, Hofmann-type CP, $M(L)_nM'(CN)_4 \cdot G$ (M = transition metal ions, L = monodentate or bidentate ligand, M' = Ni, Pd or Pt, and G = guest molecules), consists of 2D extended metal cyanide sheets made up of square-planar $[M'(CN)_4]^{2-}$ centres equatorially connected with octahedral $M(II)$ sites. [35,36] Due to the intrinsic anisotropy, Hofmann-type CP tends to form a 2D sheet-like nanostructure [37,38]. Furthermore, the removal of ligand from the parent Hofmann-type CP could effectively create numerous nanopores within its derived product. Therefore, it is envisaged that noble metal-based CP nanosheets would be ideal precursors for the fabrication of noble metal-based porous nanosheets.

As a proof of concept, herein we demonstrate a novel CP nanosheet-engaged approach to synthesize porous Pd nanosheets through sequential topotactic conversions for boosting the electrocatalysis of small molecules (Fig. 2). A Hofmann-type CP of $Pd(H_2O)_2[Ni(CN)_4] \cdot xH_2O$ with square plate-like nanostructure was firstly synthesized through a feasible hydrothermal approach, and used as template to regulate the morphology and size of target product. Afterwards, the pre-fabricated CP nanoplates were readily transformed into porous Pd-Ni oxide nanoplates upon a mild calcination. Finally, the as-synthesized porous Pd-Ni oxide nanoplates were subject to the repeated cyclic voltammetry (CV) treatments in 0.5 M H_2SO_4 solution to selectively dissolve NiO species and simultaneously electrochemically reduce the Pd oxide species into metallic Pd, resulting in the formation of porous Pd nanosheets. Remarkably, thanks to the highly open porous structure, which provides high density surface Pd atoms and easy molecular accessibility throughout the unique nanostructure, the porous Pd square nanosheets deliver extraordinary electrocatalytic properties for both the electrooxidation of liquid fuels (CH_3OH and $HCOOH$) and the oxygen reduction reaction (ORR), as compared with commercial Pd black catalyst. The outstanding bifunctional electrocatalytic properties make the porous Pd square nanosheets be an efficient electrocatalyst for fuel cell devices. It is reasonable to anticipate that the present unique strategy will enlighten the rational design of noble metal-based porous nanosheets for diverse applications.

2. Experimental

2.1. Reagents and chemicals

Potassium tetrachloropalladate(II) (K_2PdCl_4), potassium hexacyanonickelate(III) ($K_2Ni(CN)_4$) and sulfuric acid (H_2SO_4) were purchased from Sinopharm Chemical Reagent Co., Ltd (Shanghai, China). All the other reagents were of analytical grade and used without further purification. All of the aqueous solutions were prepared using Millipore water with a resistivity of $18.2\text{ M}\Omega$.

2.2. Preparation of $Pd(H_2O)_2[Ni(CN)_4] \cdot xH_2O$ square nanoplates

In a typical synthesis, 5 mL of 50 mM K_2PdCl_4 and 5 mL of 50 mM $K_2Ni(CN)_4$ aqueous solutions were mixed at room temperature. After 20 min, the light yellow $K_2PdCl_4/K_2Ni(CN)_4$ cyanogel was formed. Then, the resultant cyanogel was transferred to a 15 mL Teflon-lined stainless steel autoclave and heated at 160 °C for 1 h. After being cooled to room temperature, the light blue product was separated by centrifugation, washed with water and then dried at 40 °C in a vacuum oven for 12 h.

2.3. Preparation of Pd-Ni oxide porous nanoplates

For the synthesis of Pd-Ni oxide porous nanoplates, 40 mg of the as-synthesized $Pd(H_2O)_2[Ni(CN)_4] \cdot xH_2O$ nanoplates were placed into a crucible and calcined at 340 °C for 1 h with a heating rate of $1\text{ }^{\circ}\text{C min}^{-1}$ in air. The Pd-Ni oxide porous nanoplates were obtained after cooling to room temperature.

2.4. Preparation of porous Pd square nanosheets

The preparation of porous Pd square nanosheets was carried out in standard three-electrode system on a CHI 760 D electrochemical analyzer (CH Instruments, Shanghai, Chenhua Co.). The glassy carbon electrode (GCE) (5 mm in diameter) deposited with Pd-Ni oxide was used as a working electrode. A saturated calomel electrode (SCE) protected by Luggin capillary with KCl solution and a Pt wire were used as reference and counter electrode, respectively. In a typical synthesis, 2.0 mg of the as-obtained Pd-Ni oxide porous nanoplates were

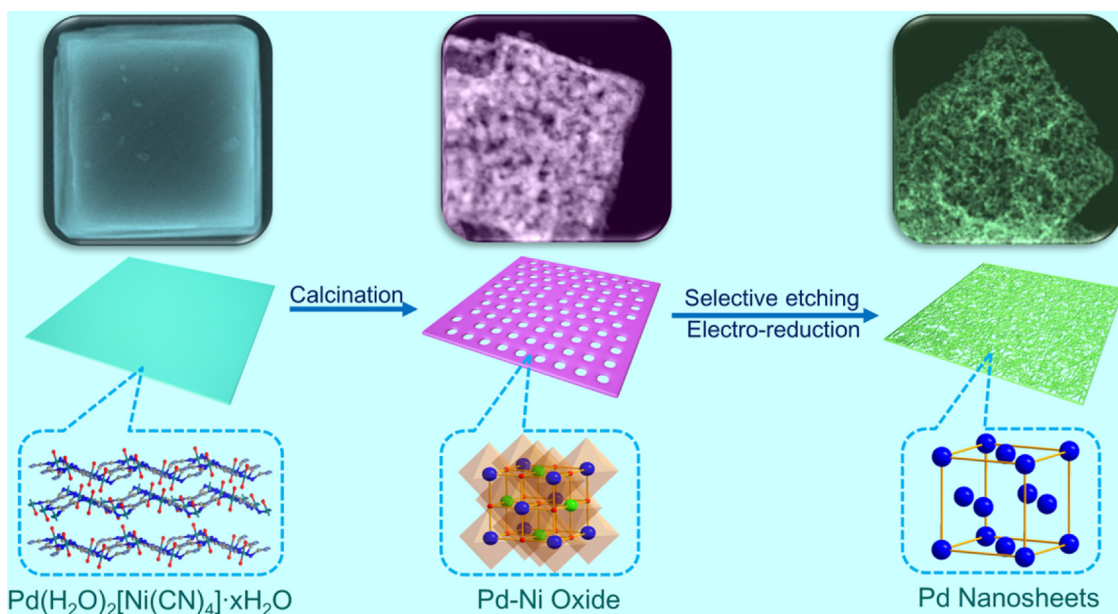


Fig. 2. Schematic demonstration of the synthesis process for the porous Pd square nanosheets.

homogeneously dispersed in 1 mL of diluted Nafion solution, which contains 0.9 mL of deionized water and 0.1 mL of 0.5 wt.% Nafion solution. Then, 6 μ L of the above suspension was dropped onto the pre-polished GCE. After drying, the oxide modified GCE electrode was performed CV in N_2 -saturated 0.5 M H_2SO_4 solution (0–1.2 V vs. reversible hydrogen electrode (RHE)) with a sweep rate of 50 mV s^{-1} at 30 °C. After 20 cycles, porous Pd square nanosheets could be obtained.

2.5. Physical characterization

The crystal phase of the products were studied by X-ray diffraction (XRD) on a Model D/max-rC X-ray diffractometer with Cu $\text{K}\alpha$ radiation source ($\lambda = 0.15406$ nm) and operating at 40 kV and 100 mA. The morphology and particle size of the samples were examined by transmission electron microscopy (TEM, JEOL JEM-2100 F) and scanning transmission electron microscopy (SEM, Hitachi S-4800). Energy dispersive spectrum (EDS), high-angle annular dark-field scanning transmission electron microscopy (HAADF-STEM), energy-dispersive X-ray (EDX) line scanning and elemental mapping measurements were performed on an FEI Tecnai G2 F20 microscope, which was built as an accessory on the JEOL JEM-2100 F. Thermogravimetric analysis (TGA) was conducted on a Netzsch STA 449C thermal analyser at a heating rate of 10 °C min^{-1} under air atmosphere. Fourier transform infrared (FT-IR) spectrum was acquired a Nicolet 520 SXFTIR spectrometer.

2.6. Electrochemical measurements

The porous Pd square nanosheet-modified electrode was used to electrocatalyze formic acid oxidation reaction (FAOR), methanol oxidation reaction (MOR) and ORR. For comparison, commercial Pd black catalyst (from Johnson Matthey Company) was used as a reference catalyst. All electrochemical tests were performed on the three-electrode system, which was previously mentioned for the preparation of porous Pd square nanosheets. The FAORs were performed in N_2 -saturated 0.5 M H_2SO_4 + 0.5 M HCOOH solution with a scan rate of 50 mV s^{-1} . For CO-stripping tests, CO was pre-adsorbed on the surface of the catalyst by bubbling CO into a 0.5 M H_2SO_4 solution while holding the working electrode at 0 V vs. SCE for 15 min. The remnant CO was driven away by flowing N_2 for 20 min before CO-stripping tests. The MOR measurements were carried out in N_2 -saturated 1.0 M KOH + 1.0 M CH_3OH solution with a scan rate of 50 mV s^{-1} . For ORR tests, a rotating

disk electrode (RDE) or rotating ring-disk electrode (RRDE) was used as the working electrode. The ORRs were conducted in O_2 -saturated 0.1 M KOH solution with a sweep rate of 5 mV s^{-1} . The electron transfer number (n) is calculated based on the equation of $n = 4I_d/(I_d + (I_r/N))$, where I_d and I_r stand for the disk current and ring current, respectively, and N is the current collection efficiency of the Pt ring (0.38).

3. Results and discussion

3.1. Formation process and characterizations of the porous Pd square nanosheets

For the typical synthesis of Hofmann-type CP nanosheets, 5 mL of 0.05 M K_2PdCl_4 and 5 mL of 0.05 M $K_2Ni(CN)_4$ aqueous solutions were initially mixed at room temperature, forming light yellow $K_2PdCl_4/K_2Ni(CN)_4$ cyanogel in 20 min (Fig. S1). The resultant cyanogel was then hydrothermally treated at 160 °C for 1 h, generating a light blue product. The crystal structure of obtained product was identified by XRD pattern (Fig. 3a). All diffraction peaks correspond well to the Hofmann-type CP of $Pd(H_2O)_2[Ni(CN)_4] \cdot xH_2O$ with an intrinsic 2D layered structure, in accordance with the previously reported studies. [37,39] No impurity phases can be detected, implying the high purity of the product. In FT-IR spectrum (Fig. S2), the presence of characteristic stretching peak of the $C\equiv N$ (2185 cm^{-1}) and the absorption peak of $Pd-CN-Ni$ (434 cm^{-1}) further validates the formation of $Pd(H_2O)_2[Ni(CN)_4] \cdot xH_2O$. [40] A typical field-emission scanning electron microscopy (FESEM) image (Fig. 3b) proves that the product predominantly constitutes of 2D square nanoplates with the lateral size in the range of 0.4–1.0 μ m. Interestingly, closer observation (inset of Fig. 3b) indicates that the nanoplates tend to stack together through a plane-to-plane manner to form multilayered structures. From the side view of the multilayered structures, the average thickness of the prepared nanoplates is estimated to be ~ 18 nm. The high-magnification FESEM image (Fig. 3c) clearly demonstrates that the square nanoplates possess a smooth surface. TEM image (Fig. 3d) verifies the plate-like structure of the as-prepared product. The brightness contrast in the rim region of the TEM image (Fig. 3e) further validates that the nanoplates tend to stack together to form multilayered structures, being in line with the above FESEM results. Selected-area electron diffraction (SAED) pattern (Fig. 3f) of the nanoplates implies the single-crystalline feature of the square nanoplates. High-angle annular dark-field scanning TEM image

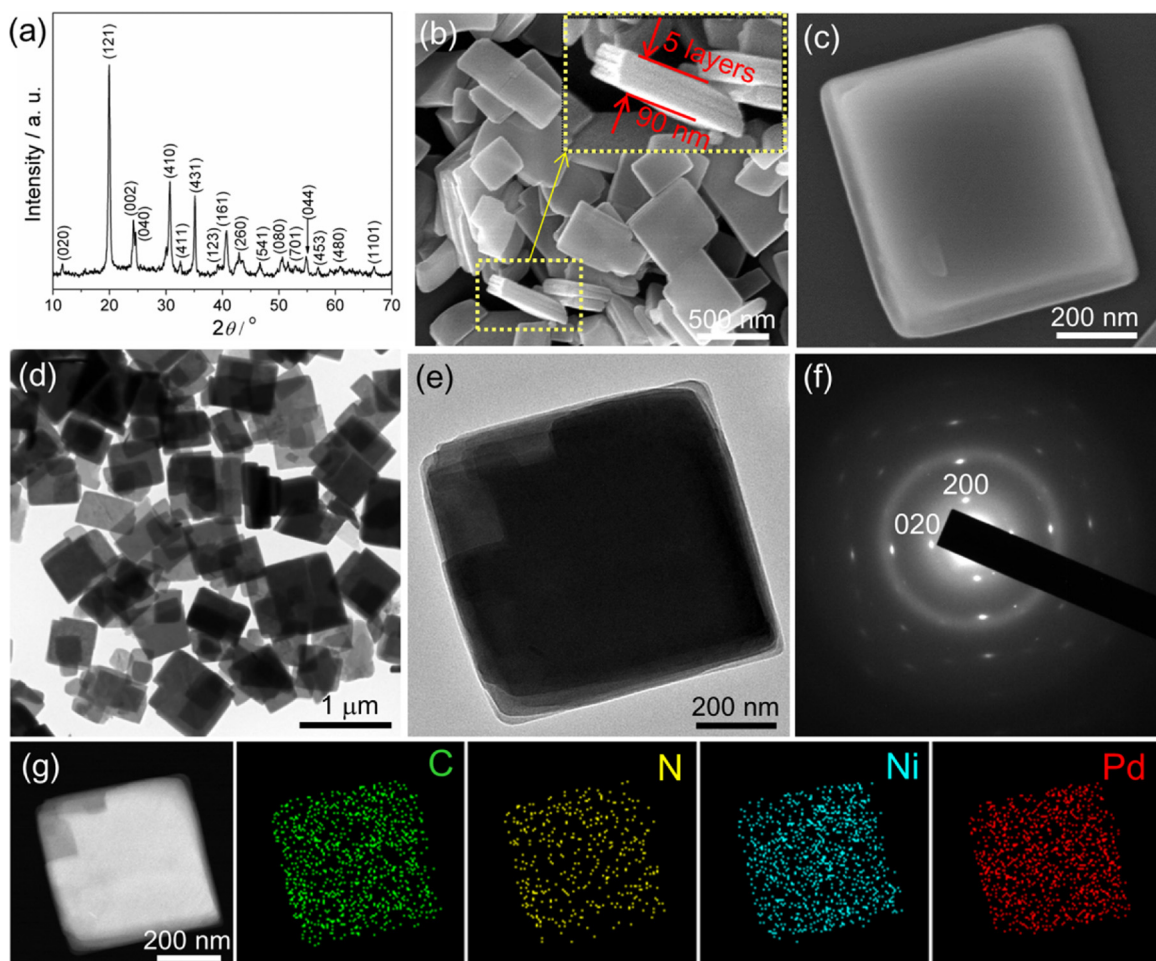


Fig. 3. (a) XRD pattern, (b, c) SEM images, (d, e) TEM images, (f) SAED pattern, (g) HAADF-STEM images and elemental mapping images of the $\text{Pd}(\text{H}_2\text{O})_2[\text{Ni}(\text{CN})_4] \cdot x\text{H}_2\text{O}$ square nanoplates.

(Fig. 3g) further corroborate that the sample is made up of 2D square multilayer nanoplates with high yield. Elemental mapping images imply that the elements of Pd, Ni, N and C are distributed homogeneously through the entire square nanoplates. The chemical compositions of the nanoplates are further examined by EDS, where both Pd and Ni elements are found to be incorporated within the nanoplates with the Pd/Ni atomic ratio of $\sim 1:1$ (Fig. S3). TGA in Fig. S4 indicates that the as-synthesized CP dehydrates to remove the adsorbed free water and coordinated water in the temperature range of 100–240 °C, and starts to decompose at 340 °C.

According to decomposition point obtained from the TGA analysis, the as-prepared CP nanoplates were calcinated at 340 °C under air atmosphere for 1 h. As evidenced by XRD pattern (Fig. S5), the CP nanoplates were completely transformed into Pd-Ni oxide after the calcination treatment. From the TEM images (Fig. S6a and b), one can clearly see that the oxide inherits the 2D square plate-like morphology of the CP template while the nanoplates become highly porous, suggesting the formation of plenty of pores during the annealing process. The HAADF-STEM image (Fig. S6c) of one individual oxide nanoplate further validates the rough and porous feature of the as-obtained oxide nanoplates. The corresponding elemental mapping analysis confirms the co-existence and homogenous distribution of Pd, Ni and O throughout the whole porous nanoplate. And the corresponding EDS analysis (Fig. S7) of the obtained oxide shows the Pd/Ni atomic ratio of $\sim 1:1$, which is identical to that in the CP precursor.

CV process was then employed to treat the as-prepared porous Pd-Ni oxide nanoplates in N_2 -saturated 0.5 M H_2SO_4 solution, in order to

selectively leach Ni oxide out and simultaneously reduce Pd oxide into metallic Pd. Upon exposure to H_2SO_4 medium, Ni oxide species would be dissolved through a selective chemical etching process. Meanwhile, Pd oxide could be electrochemically reduced to metallic Pd(0) through multiple cycles in the potential range of 0–1.2 V vs. RHE. Fig. S8 illustrates the typical CV curves during the electrochemical reduction processes. The CV curve of the first cycle exhibits neither appreciable hydrogen adsorption/desorption peaks between 0 and 0.3 V nor noticeable reduction peak of Pd oxide during the cathodic scan. As the cycling proceeds, well-defined peaks of hydrogen adsorption/desorption and formation of Pd oxide species (~ 0.7 V) increase steadily as the CV cycling numbers increase. In addition, both of the onset and the peak potentials for the Pd oxide reduction shift positively with cycling, which may be ascribed to the growth and ripening of the generated Pd nanoparticles. After 20 CV cycles, the CV curve becomes stable and agrees well with the typical features of Pd in H_2SO_4 solution, indicating the complete reduction of Pd oxide into metallic Pd. [41–43]

After the above one-step chemical etching and electrochemical reduction treatment, the morphology and detailed structure of the resultant sample were further investigated. XRD pattern (Fig. 4a) shows the diffraction peaks of a face-centered cubic (fcc)-phased metallic Pd. Neither signals for PdO nor NiO phase can be observed, suggesting the complete transformation of Pd-Ni oxide into Pd. A representative TEM image (Fig. 4b) indicates that the overall porous 2D square plate-like structure was well maintained after the electrochemical reduction treatment. A magnified TEM image (Fig. 4c) of one individual porous Pd nanosheet illustrates that the porosity of this Pd nanosheets is more

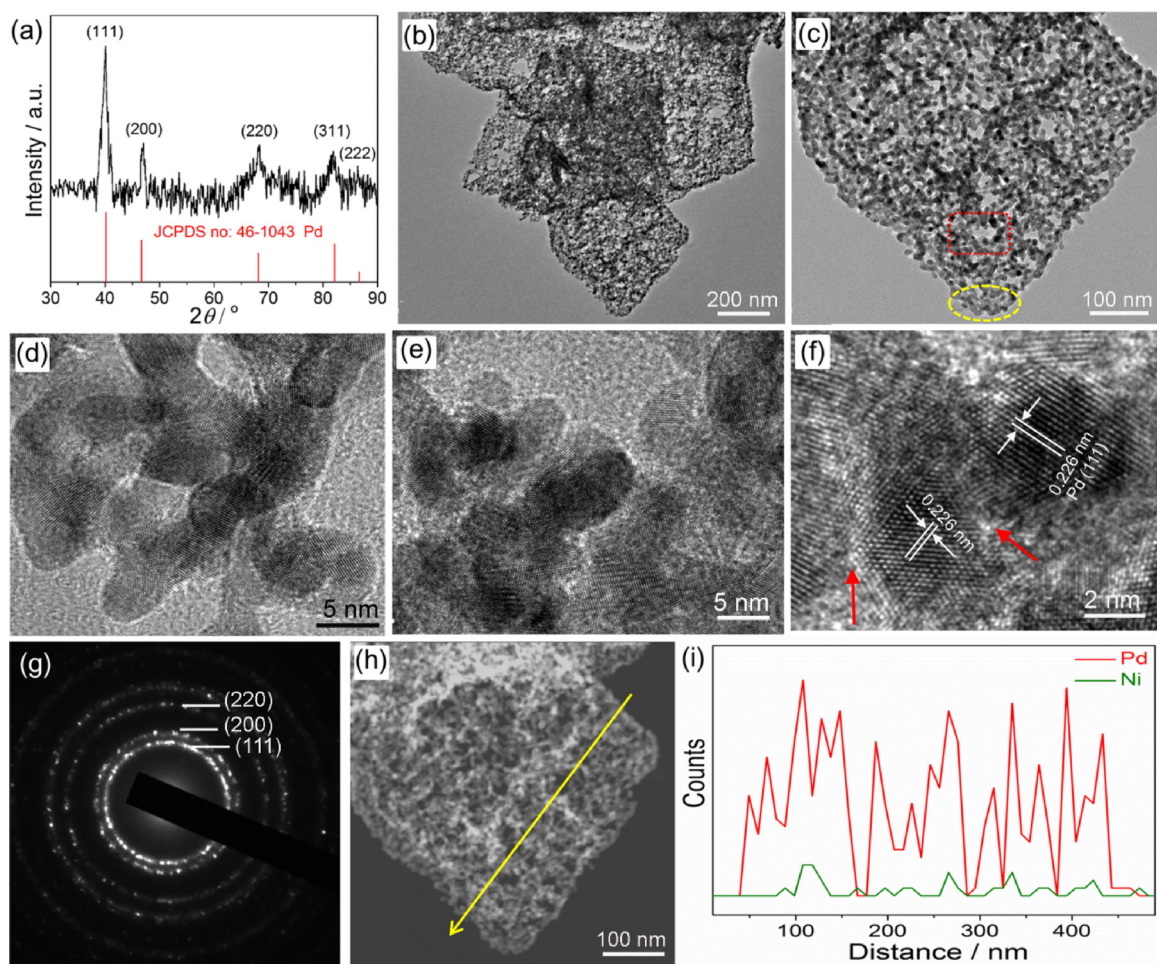


Fig. 4. Compositional and structural characterization of the prepared porous Pd square nanosheets. (a) XRD, (b, c) TEM images, (d, e) magnified TEM images taken from the areas marked in panel c, (f) HRTEM image, (g) SAED pattern, (h) HAADF-STEM image and (i) EDX cross-sectional line scan profiles.

obvious than that of the parent oxide nanosheets. Such rich porosity can greatly improve the surface-to-volume ratio and thus effectively promote the electrocatalytic activity. As marked by the yellow circle and red frame in Fig. 4c, closer TEM observations on the edge (Fig. 4d) and central region (Fig. 4e) of the porous Pd nanosheets provide more structural details, indicating that the Pd porous nanosheets are essentially constructed by networked nanoligaments with size in the range of 4~7 nm. As shown in HRTEM image of two neighboring nanoparticles in the ligament (Fig. 4f), well-resolved lattice fringes are identified to be 0.226 nm, ascribing to the Pd (111) planes. It should be noted that the lattice fringes of (111) planes are not continuous along the same direction due to the varied orientation of the constituent nanoparticles. Furthermore, the nanoligaments show a highly rough surface with rich corner and edge atoms, as marked by arrows in Fig. 4f. These corner and edge atoms could act as catalytically active sites, and are expected to boost the catalytic activities. [44] The corresponding SAED pattern (Fig. 4g) implies the polycrystalline nature of the porous Pd square nanosheets, and the diffraction rings can be assigned to the (111), (200), and (220) planes of fcc-phased Pd, respectively. In agreement with the TEM observation, the HAADF-STEM image (Fig. 4h) further manifests the highly porous structure with a sharp contrast between the bright Pd nanoligaments and dark pores. The EDX line scan profile (Fig. 4i) shows that Pd is in the dominant position in the composition of the porous Pd square nanosheets with only trace amount of remaining Ni, further verifying the successful removal of Ni. This result is strongly supported by the elemental mapping and EDS analysis, as shown in Fig. S9.

More importantly, the present CP-derived protocol could also be

extended to fabricate Pt and Au porous nanosheets by utilizing PtNi-based and AuNi-based CP nanosheets as precursors. As shown in Fig. S10, Pt and Au nanosheets with high porosity can be harvested through the similar topochemical reactions after appropriate annealing and electrochemical reduction processes, demonstrating the generality and versatility of this synthetic strategy.

3.2. Electrocatalytic performances of the porous Pd square nanosheets

In view of the highly open and porous structure as well as the small crystallite size, the fabricated porous Pd square nanosheets are reasonably anticipated to exhibit outstanding electrocatalytic performance. Therefore, the electrocatalytic properties of the porous Pd square nanosheets for oxygen reduction reaction were evaluated. For comparison, commercial Pd black catalyst was employed as a benchmark under the identical experimental conditions. Fig. S11 presents the typical CV curves of the two catalysts in a N₂-saturated 0.5 M H₂SO₄ solution, respectively. According to the integrated charges for the reduction of PdO monolayer during the cathodic scan, [17,45,46] the electrochemically active surface area (ECSA) of the porous Pd square nanosheets is calculated to be 22.4 m² g⁻¹, which is 3.1 times larger than that of the Pd black (7.2 m² g⁻¹). The remarkable increase of ECSA of the porous Pd nanosheets should be due to its porous feature and the small crystallite size of the nanoligaments. Fig. 5a presents the typical ORR polarization plots of the two catalysts recorded in O₂-saturated 0.1 M KOH solution. The half-wave potential ($E_{1/2}$) for the porous Pd square nanosheets is determined to be 0.837 V, which positively shifts ~15 mV relative to the commercial Pd black, suggesting excellent ORR

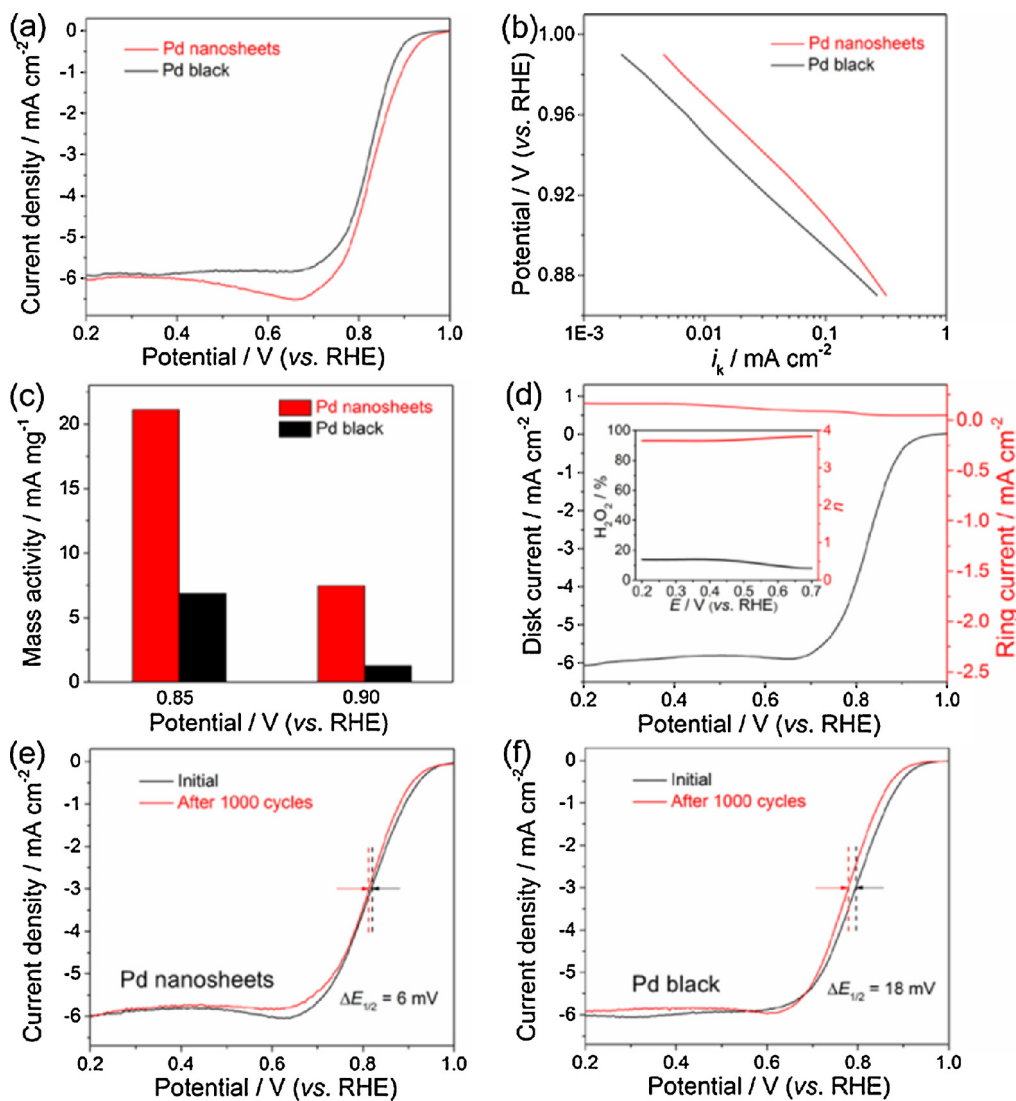


Fig. 5. ORR performances of porous Pd square nanosheets and commercial Pd black catalyst. (a) ORR polarization plots recorded in an O₂-saturated 0.1 M KOH solution (scan rate: 5 mV s⁻¹, and rotation rate: 1600 rpm), (b) Tafel plots, (c) comparison of kinetic mass activities of ORR at 0.85 and 0.90 V vs. RHE. (d) The current collected on disk and ring electrodes catalyzed by porous Pd square nanosheets. Inset: H₂O₂ yield and electron number transferred in ORR. (e, f) ORR polarization plots of porous Pd square nanosheets and Pd black after 1000 cycles.

activity of the porous Pd square nanosheets. The corresponding Tafel plots (Fig. 5b) manifest that the kinetic current density (i_k) of porous Pd square nanosheets is remarkably larger than that of the commercial Pd black. The mass activity comparison of the two catalysts at 0.85 and 0.90 V is displayed in Fig. 5c. The porous Pd square nanosheets exhibit a mass activity of 21.1 mA mg⁻¹ at 0.85 V, which is greater than that of Pd black (6.8 mA mg⁻¹) by a factor of 3.1. Likewise, the mass activity of the porous Pd square nanosheets at 0.9 V is 5.9 times higher than that of Pd black.

To further study the ORR pathway of the porous Pd square nanosheets, the formation of peroxide species (HO₂[·]) was examined by RRDE measurement (Fig. 5d) during the ORR process. Inset of Fig. 5d suggests that, for the Pd square nanosheets, the peroxide yield during the ORR is quite low (< 10%) and the electron transfer number (n) ranges from 3.73 to 3.85. The RRDE result reveals that a favorable four-electron-pathway is dominated in the ORR process catalyzed by porous Pd square nanosheets. Accelerated durability tests (ADTs) for 1000 cycles were conducted to assess the ORR stability of the two catalysts (Fig. 5e and f). Apparently, the degradation degree of porous Pd square nanosheets is significantly lower than that of commercial Pd black, as evidenced by the negligible negative shift in $E_{1/2}$ (6 mV vs. 18 mV),

indicating the excellent stability of porous Pd square nanosheets toward ORR.

Impressively, the porous Pd square nanosheets also exhibit efficient electrooxidation performance of small molecules (formic acid and methanol) with high activity and stability. Fig. S12a displays the mass-normalized FAOR CVs of the two catalysts. Obviously, the onset potential for FAOR on our porous Pd square nanosheets is much more negative than that of commercial Pd black, indicating a favorable FAOR on the synthesized Pd square nanosheets. Moreover, the mass-normalized peak current density of FAOR on our porous Pd nanosheets (665.9 A g⁻¹) is 3.33 times significantly higher than that of the Pd black, demonstrating a greatly enhanced FAOR activity (Fig. S12c). The porous Pd square nanosheets also exhibit superior catalytic efficiency toward methanol oxidation reaction with much negative onset potential and considerably improved peak current density, as illustrated in Fig. S12b. The peak current density of MOR is 2.71 times greater than that on Pd black (596.8 vs. 220.3 A g⁻¹). As reflected by the CO-stripping CVs (Fig. S12d), the resultant porous Pd square nanosheets exhibit more negative onset potential and the peak potential of CO oxidation as compared with commercial Pd black, revealing the better anti-poisoning capability of the porous Pd square nanosheets [47].

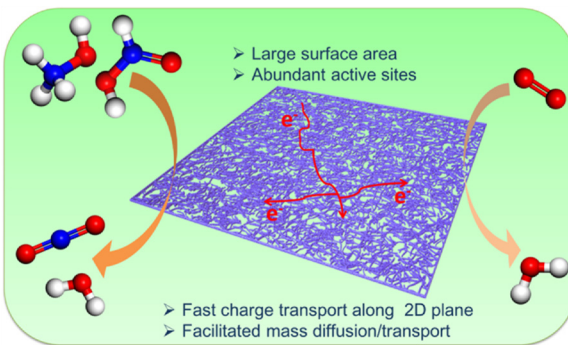


Fig. 6. A schematic illustration of the structural merits of the porous Pd square nanosheets as an efficient bifunctional electrocatalyst.

Chronoamperometry (CA) tests were implemented in 0.5 M H_2SO_4 + 0.5 M HCOOH solution at 0.35 V for 3000 s. As displayed by the CV curves in Fig. S12e, the current attenuation on the porous Pd square nanosheets is noticeably slower than that on the commercial Pd black catalyst, affirming that the porous Pd square nanosheets exhibit a higher CO tolerance capability. In addition, the current density for FAOR on the prepared Pd nanosheets is noticeably larger than that on the Pd black during the whole measurement, demonstrating the excellent activity and stability of the Pd square nanosheets. Additionally, as depicted by the TEM image in Fig. S12f, the porous Pd square nanosheets could well retain their initial 2D porous morphology after the CA test, without appreciable aggregation or dissolution. While, in contrast, commercial Pd black catalyst aggregated severely after the stability measurement (Fig. S13).

The enhanced catalytic activity and stability for both electrooxidation of liquid molecules and ORR of the porous Pd square nanosheets can be ascribed to their unique structural features, as highlighted in Fig. 6. Specifically, (1) the highly open and porous structure endows the catalyst sufficient accessible active sites and high atom utilization efficiency; (2) the abundant edges and corner atoms resulting from the rough surface of the nanoligaments are advantageous to improve the electrocatalytic activity; (3) unlike the conventional 2D nanosheets with smooth and intact surface, the large void space within the porous nanosheets would facilitate mass diffusion and transport during the catalytic reaction, which in turn promotes the reaction kinetics; (4) the interconnected nanoligaments and the square sheet-like nanostructures could not only provide direct path for electron transfer, but also make these unique Pd nanosheets less susceptible to dissolution, Ostwald ripening, and agglomeration as compared with the 0D counterpart [48]. Furthermore, the synergy between trace Ni and Pd may also make certain contribution to the improved catalytic activities due to the modification of Pd electronic structure.

4. Conclusion

In summary, for the first time, we have elaborately designed a novel CP-templated strategy to synthesize porous Pd square nanosheets. The CP templates of $\text{Pd}(\text{H}_2\text{O})_2[\text{Ni}(\text{CN})_4] \cdot x\text{H}_2\text{O}$ with square plate-like structure undergo thermal decomposition and electrochemical reduction as well as simultaneous selective dissolution of Ni species, finally transforming into porous Pd square nanosheets. Notably, this CP-engaged protocol can be potentially extendable to synthesize other noble metal porous nanosheets due to its feasibility and versatility. Through sequential topochemical reactions, the morphology and size of the final derived metal porous nanosheets can be readily manipulated by tailoring the structural parameters of the preformed CP precursors with well-defined morphology. Thanks to the unique highly open and porous structure, the as-prepared porous Pd square nanosheets served as highly efficient bifunctional electrocatalysts in both the electrooxidation of liquid fuels (methanol and formic acid) and ORR with greatly improved

activity and durability than the commercial Pd black catalyst. Specifically, it exhibited over 2.7 and 5.9 times better mass activity for MOR and ORR, respectively, than the Pd black catalyst, suggesting a promising and versatile bifunctional catalyst candidate for fuel cells and beyond. This work not only enriches the family of CP-derived functional nanomaterials but also will offer great opportunity to rational design of 2D noble metal-based porous nanostructures with promising applications in electrochemical energy devices.

Acknowledgements

The authors are grateful for the financial supports from National Natural Science Foundation of China (21503111 and 21576139), Natural Science Foundation of Jiangsu Higher Education Institutions of China (16KJB150020), Natural Science Foundation of Jiangsu Province (BK20171473), Natural Sciences and Engineering Research Council of Canada (NSERC) and China Scholarship Council (CSC, No. 201706860019). The authors also thank National and Local Joint Engineering Research Center of Biomedical Functional Materials and a project sponsored by the Priority Academic Program Development of Jiangsu Higher Education Institutions.

Appendix A. Supplementary data

Supplementary material related to this article can be found, in the online version, at doi:<https://doi.org/10.1016/j.apcatb.2018.10.028>.

References

- [1] T. Ling, J.J. Wang, H. Zhang, S.T. Song, Y.Z. Zhou, J. Zhao, X.W. Du, *Adv. Mater.* 27 (2015) 5396–5402.
- [2] J.P. Lai, S.J. Guo, *Small* 13 (2017) 1702156.
- [3] L.Z. Bu, N. Zhang, S.J. Guo, X. Zhang, J. Li, J. Yao, T. Wu, G. Lu, J.Y. Ma, D. Su, X. Huang, *Science* 354 (2016) 1410–1414.
- [4] H.H. Duan, N. Yan, R. Yu, C.R. Chang, G. Zhou, H.S. Hu, H.P. Rong, Z.Q. Niu, J.J. Mao, H. Asakura, *Nat. Commun.* 5 (2014) 3093.
- [5] Y.G. Sun, C.H. Lei, *Angew. Chem. Int. Ed.* 48 (2009) 6824–6827.
- [6] H.P. Liu, P. Zhong, K. Liu, L. Han, H.Q. Zheng, Y.D. Yin, C.B. Gao, *Chem. Sci.* 9 (2018) 398–404.
- [7] X.Q. Huang, S.H. Tang, X.L. Mu, Y. Dai, G.X. Chen, Z.Y. Zhou, F.X. Ruan, Z.L. Yang, N.F. Zheng, *Nat. Nanotechnol.* 6 (2011) 28–32.
- [8] B.A. Larsen, K. Neyerlin, J.B. Bult, C. Bochert, J.L. Blackburn, S.S. Kocha, B.S. Pivovar, *J. Electrochem. Soc.* 159 (2012) F622–F627.
- [9] M. Chen, S.H. Tang, Z.D. Guo, X.Y. Wang, S.G. Mo, X.Q. Huang, G. Liu, N.F. Zheng, *Adv. Mater.* 26 (2014) 8210–8216.
- [10] W.J. Fang, S.H. Tang, P.X. Liu, X.L. Fang, J.W. Gong, N.F. Zheng, *Small* 8 (2012) 3816–3822.
- [11] A.X. Yin, W.C. Liu, J. Ke, W. Zhu, J. Gu, Y.W. Zhang, C.H. Yan, *J. Am. Chem. Soc.* 134 (2012) 20479–20489.
- [12] Y. Li, W.X. Wang, K.Y. Xia, W.J. Zhang, Y.Y. Jiang, Y.W. Zeng, H. Zhang, C.H. Jin, Z. Zhang, D.R. Yang, *Small* 11 (2015) 4745–4752.
- [13] Y.T. Pan, X. Yin, K.S. Kwok, H. Yang, *Nano Lett.* 14 (2014) 5953–5959.
- [14] Y.W. Zhang, G.H. Chang, S. Liu, W.B. Lu, J.Q. Tian, X.P. Sun, *Biosens. Bioelectron.* 28 (2011) 344–348.
- [15] X. Hong, C.L. Tan, J.Q. Liu, J. Yang, X.J. Wu, Z.X. Fan, Z.M. Luo, J.Z. Chen, X. Zhang, B. Chen, *J. Am. Chem. Soc.* 137 (2015) 1444–1447.
- [16] F. Saleem, B. Xu, B. Ni, H.L. Liu, F. Nosheen, H.Y. Li, X. Wang, *Adv. Mater.* 27 (2015) 2013–2018.
- [17] X.Y. Qiu, H.Y. Zhang, P.S. Wu, F.Q. Zhang, S.H. Wei, D.M. Sun, L. Xu, Y.W. Tang, *Adv. Funct. Mater.* 27 (2017) 1603852.
- [18] X. Huang, S.Z. Li, Y.Z. Huang, S.X. Wu, X.Z. Zhou, S.Z. Li, C.L. Gan, F. Boey, C.A. Mirkin, H. Zhang, *Nat. Commun.* 2 (2011) 292.
- [19] J. Tiwari, C.R. Rao, *Solid State Ionics* 179 (2008) 299–304.
- [20] L. Zhao, C.F. Xu, H.F. Su, J.H. Liang, S.C. Lin, L. Gu, X.L. Wang, M. Chen, N.F. Zheng, *Adv. Sci. S.* 2 (2015) 1500100.
- [21] Q. Zhang, Y.X. Hu, S.R. Guo, J. Goebel, Y.D. Yin, *Nano Lett.* 10 (2010) 5037–5042.
- [22] R.C. Jin, Y.W. Cao, C.A. Mirkin, K.L. Kelly, G.C. Schatz, J.G. Zheng, *Science* 294 (2001) 1901–1903.
- [23] Q. Zhang, J.P. Ge, T. Pham, J. Goebel, Y.X. Hu, Z.D. Lu, Y.D. Yin, *Angew. Chem.* 121 (2009) 3568–3571.
- [24] A.U. Khan, Z.P. Zhou, J. Krause, G.L. Liu, *Small* 13 (2017) 1701715.
- [25] Z.N. Wu, C.W. Dong, Y.C. Li, H.X. Hao, H. Zhang, Z.Y. Lu, B. Yang, *Angew. Chem. Int. Ed.* 52 (2013) 9952–9955.
- [26] X.K. Kong, K. Xu, C.L. Zhang, J. Dai, S. Norooz Oliaee, L.Y. Li, X.C. Zeng, C.Z. Wu, Z.M. Peng, *ACS Catal.* 6 (2016) 1487–1492.
- [27] L. Yu, B.Y. Guan, W. Xiao, X.W. Lou, *Adv. Energy Mater.* 5 (2015) 1500981.
- [28] X.N. Li, J.Y. Liu, A.I. Rykov, H.X. Han, C.Z. Jin, X. Liu, J.H. Wang, *Appl. Catal. B*

Environ. 179 (2015) 196–205.

[29] L. Han, X.Y. Yu, X.W. Lou, *Adv. Mater.* 28 (2016) 4601–4605.

[30] F.X. Bu, M. Hu, W. Zhang, Q. Meng, L. Xu, D.M. Jiang, J.S. Jiang, *Chem. Commun.* 51 (2015) 17568–17571.

[31] B. Kong, J. Tang, Z.X. Wu, C. Selomulya, H.T. Wang, J. Wei, Y.C. Wang, G.F. Zheng, D.Y. Zhao, *NPG Asia Mater.* 6 (2014) e117.

[32] J.S. Lee, G. Nam, J. Sun, S. Higashi, H.W. Lee, S. Lee, W. Chen, Y. Cui, J. Cho, *Adv. Energy Mater.* 6 (2016) 1601052.

[33] X.Y. Yu, L. Yu, H.B. Wu, X.W. Lou, *Angew. Chem. Int. Ed.* 54 (2015) 5331–5335.

[34] X.Y. Yu, Y. Feng, B.Y. Guan, X.W. Lou, U. Paik, *Energy Environ. Sci.* 9 (2016) 1246–1250.

[35] F.J. Valverde-Muñoz, M. Seredyuk, M.C. Muñoz, K. Znoviyak, I.O. Fritsky, J.A. Real, *Inorg. Chem.* 55 (2016) 10654–10665.

[36] V. Niel, J.M. Martinez-Agudo, M.C. Muñoz, A.B. Gaspar, J.A. Real, *Inorg. Chem.* 40 (2001) 3838–3839.

[37] M. Hu, S. Ishihara, Y. Yamauchi, *Angew. Chem. Int. Ed.* 52 (2013) 1235–1239.

[38] H.S. Fan, H. Yu, X.L. Wu, Y. Zhang, Z.Z. Luo, H.W. Wang, Y.Y. Guo, S. Madhavi, Q.Y. Yan, *ACS Appl. Mater. Interfaces* 8 (2016) 25261–25267.

[39] E. Ruiz, S. Alvarez, R. Hoffmann, J. Bernstein, *J. Am. Chem. Soc.* 116 (1994) 8207–8221.

[40] Z.Y. Liu, G.T. Fu, L. Zhang, X.Y. Yang, Z.Q. Liu, D.M. Sun, L. Xu, Y.W. Tang, *Sci. Rep.* 6 (2016) 32402.

[41] L.G. Feng, S.K. Yao, X. Zhao, L. Yan, C. Liu, W. Xing, *J. Power Sources* 197 (2012) 38–43.

[42] L.G. Feng, J.F. Chang, K. Jiang, H.G. Xue, C.P. Liu, W.B. Cai, W. Xing, J.J. Zhang, *Nano Energy* 30 (2016) 355–361.

[43] D. Liu, M.L. Xie, C.M. Wang, L.W. Liao, L. Qiu, J. Ma, H. Huang, R. Long, J. Jiang, Y.J. Xiong, *Nano Res.* 9 (2016) 1590–1599.

[44] X. Jiang, X.X. Yan, W.Y. Ren, Y.F. Jia, J.N. Chen, D.M. Sun, L. Xu, Y.W. Tang, *ACS Appl. Mater. Interfaces* 8 (2016) 31076–31082.

[45] S.Z. Hu, F. Munoz, J. Noborikawa, J. Haan, L. Scudiero, S. Ha, *Appl. Catal. B: Environ.* 180 (2016) 758–765.

[46] L. Zhang, L. Wan, Y.R. Ma, Y. Chen, Y.M. Zhou, Y.W. Tang, T.H. Lu, *Appl. Catal. B Environ.* 138 (2013) 229–235.

[47] L. Zhang, Q. Sui, T.T. Tang, Y. Chen, Y.M. Zhou, Y.W. Tang, T.H. Lu, *Electrochem. Commun.* 32 (2013) 43–46.

[48] C. Koenigsmann, A.C. Santulli, K.P. Gong, M.B. Vukmirovic, W.P. Zhou, E. Sutter, S.S. Wong, R.R. Adzic, *J. Am. Chem. Soc.* 133 (2011) 9783–9795.